Electronic Supplementary Material (ESI) for Journal of Materials Chemistry A.
This journal is © The Royal Society of Chemistry 2022

# *Supplementary Information*

## Controlled synthesis of highly active bifunctional electrocatalysts for overall water splitting using coal-based activated carbons

Xianglong Zhao,[a] Xinghua Yong,[a] Qizhe Ji,[a] Zhenghua Yang,[a] Yang Song,*[b] Yiqiang Sun,[c] Zhengyang Cai,[d] Jingcheng Xu,[e] Luyan Li,[a] Shuhua Shi,[a] Feiyong Chen,[b] Cuncheng Li,[c] Ping Wang*[d] and Jong-Beom Baek*[f]

[a]School of Science, Shandong Jianzhu University, Jinan, 250101, P. R. China

[b]Resources and Environment Innovation Institute, Shandong Jianzhu University, Jinan, 250101, P. R. China
Email: songyang20@sdjzu.edu.cn

[c]School of Chemistry and Chemical Engineering, University of Jinan, Jinan, 250022, P. R. China

[d]Energy Materials Research Center, Shanghai Institute of Ceramics, Chinese Academy of Sciences, Shanghai, 201899, P. R. China
Email: wangping@mail.sic.ac.cn

[e]School of Materials and Chemistry, University of Shanghai for Science and Technology, Shanghai, 200093, P. R. China

[f]School of Energy and Chemical Engineering/Center for Dimension-Controllable Organic Frameworks, Ulsan National Institute of Science and Technology (UNIST), Ulsan 44919, Korea
Email: jbbaek@unist.ac.kr

## Density functional theory calculations

The Vienna Ab Initio Package (VASP) was employed to perform all the spin-polarized density functional theory (DFT) calculations with the projector augmented wave (PAW) pseudo-potentials. The plane-wave basis set was defined by a kinetic energy cutoff of 500 eV, the electron exchange and correlation interactions were treated within the generalized gradient approximation (GGA) using the Perdew-Burke-Ernzerhof (PBE) functional. The k-point sampling was obtained from the Monkhorst-Pack scheme with a Gamma-centered (1×1×1) mesh. The convergence tolerances of SCF energy and force for full-relax geometry optimizations were set to be $1.0\times10^{-5}$ eV

and 0.02 eV/Å. The NCAC structure was modeled from single-layer N-modified single-vacancy graphene plane with a lattice constant of 12.27 Å × 12.27 Å, and the 15 Å vacuum layer was applied to avoid strong interactions. The $Ni_3N/Ru_6$/NCAC structure was modeled from $Ni_3N$ and $Ru_6$ cluster adsorbed on the NCAC structure, and the structure ($Ru_6$/NCAC) of only $Ru_6$ cluster adsorbed on the NCAC was constructed as contrasts.

The OER process was divided into four fundamental reactions:

$$H_2O + * \rightarrow *OH + H^+ + e^-$$

$$*OH \rightarrow *O + H^+ + e^-$$

$$*O + H_2O \rightarrow *OOH + H^+ + e^-$$

$$*OOH \rightarrow * + O_2 + H^+ + e^-$$

where *OH, *O and *OOH present the OOH, O and OH adsorbed on the adsorption site *.

The change in Gibbs free energy (ΔG) of each adsorbed intermediate was calculated based on the computational hydrogen electrode method developed by Nørskov et al.[1] At standard condition (T = 298.15 K, pH = 0, and U = 0 V (vs. SHE)), the free energy (G) is defined as the following equation:

$$\Delta G = \Delta E + \Delta ZPE - T\Delta S$$

where ΔE is the energy change obtained from DFT calculation, ΔZPE is the difference of zero-point energy between the adsorbed state and gas, T is the temperature (298.15 K), and ΔS is the difference in the entropies between the adsorbed state and gas phase.

**Experimental Section**

*Fabrication of the $Ni_3N$/Ru/NCAC composites*: First, 300 mg of CACs (purchased from Henan Huansheng Carbon Co., P. R. China) was milled into powders. Then, 1 ml of aqueous solutions containing $RuCl_3$ (0.07 M) and $NiCl_3$ (0.15 M) was dropped on the CAC powders, followed by drying. Finally, ammonia annealing was conducted at 1000 °C for 1.5 h with an ammonia flowing rate of 100 sccm.

Using a similar approach, $Ni_3N$/Ru/NWAC, $Ni_3N$/Ru/NSAC, and $Ni_3N$/Ru/NCNT composites were also prepared.

*Electrochemical measurements*: The electrochemical tests were conducted on an electrochemical workstation (CHI 760D, CH Instruments, Inc., Shanghai, China), using a standard three-electrode electrochemical cell with a Hg/HgO electrode as the reference elecrode. For OER and HER, a platinum wire and a graphite rod were used as the counter electrodes, respectively. The working electrodes were prepared by dropping catalyst ink onto a piece of carbon cloth (1 square centimeter). Briefly, samples (5 mg) were dispersed in a mixture of ethanol (900 μL) and nafion (0.5 wt%, 100 μL), followed by ultrasonication for 5 min. Then, 200 μL of catalyst ink (which contained ~ 1 mg of catalysts) was cast onto the surfaces of the carbon cloth, followed by drying. In addition, the amounts of $IrO_2$ and Pt/C loaded on the surface of the carbon cloth were also ~ 1 mg.

For the OER performance evaluation, the LSV curves were recorded in oxygen saturated 0.1 M KOH aqueous solutions at a scan rate of 5 mV $s^{-1}$. All of the measured potentials in this work were converted with reference to the standard RHE according to

the Nernst equation: $E_{RHE} = E_{Hg/HgO} + 0.059 \times pH + 0.098$. The EIS were recorded at 1.54 V vs. RHE in the frequency range of 0.1-100000 Hz with an amplitude of 5 mV. The cyclic voltammogram measurements were carried out with different scan rates from 2 to 16 mV $s^{-1}$ in a potential range from 0.96 to 1.06 V vs. RHE.

For the HER performance evaluation, the LSV curves were recorded in nitrogen saturated 1 M KOH aqueous solutions at a scan rate of 5 mV $s^{-1}$. The EIS were recorded at -0.21 V vs. RHE in the frequency range of 0.1-100000 Hz with an amplitude of 5 mV.

The OWS performances of the $Ni_3N$/Ru/NCAC composites were evaluated using a two-electrode electrolyzer with $Ni_3N$/Ru/NCAC composites as both anodes and cathodes. The LSV curves were recorded in 1 M KOH aqueous solutions at a scan rate of 5 mV $s^{-1}$. The amounts of evolved $H_2$ and $O_2$ were determined using a gas chromatograph (GC2010Plus ATF, Shimadzu).

*Characterization*: SEM was performed on a Hitachi SU8020. TEM and HRTEM were carried out on a FEI Tecnai TF20. XPS spectra were recorded on a Thermo Fisher K-alpha XPS spectrometer. XRD patterns were recorded on a Philips X-Pert Pro X-ray diffractometer with Cu-Ka radiation, and the scan rate was 2 degree/min. The nitrogen adsorption-desorption isotherms were measured on a Micromeritics ASAP2460. The ICP-MS measurement was conducted on an Agilent ICPMS 7700. The Raman spectra were measured using a laser confocal Raman spectrometer (LabRAM HR Evolution, HORIBA Jobin Yvon, France) with an excitation wavelength of 532 nm.

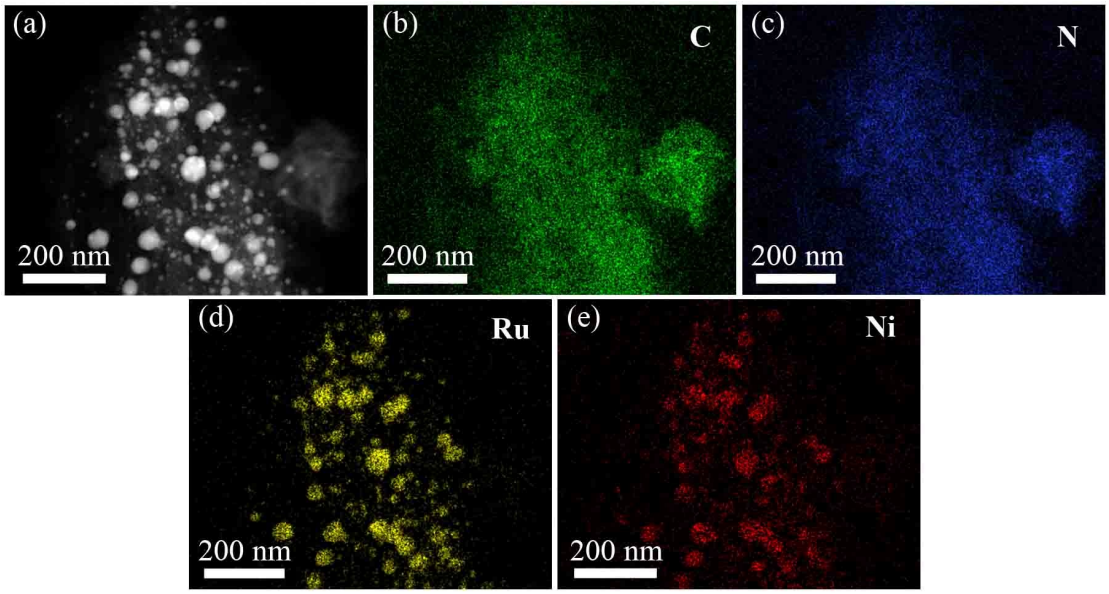


**Fig. S1** (a) TEM image of a $Ni_3N$/Ru/NCAC composite. (b)-(e) Elemental mappings from (a): (b) C, (c) N, (d) Ru, and (e) Ni.

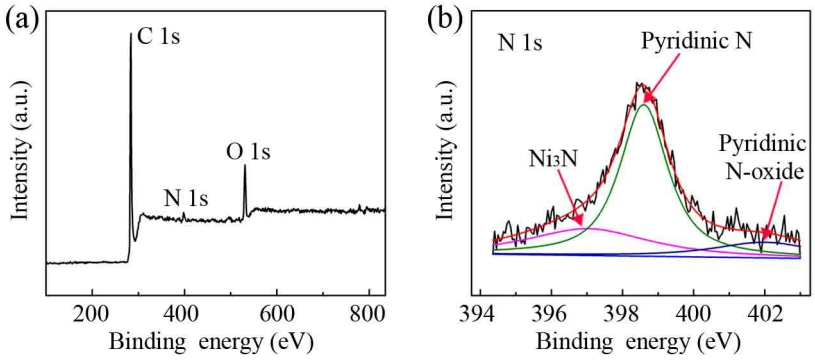


**Fig. S2** (a) XPS spectrum of the $Ni_3N$/Ru/NCAC composites. (b) High resolution XPS spectra of N 1s.

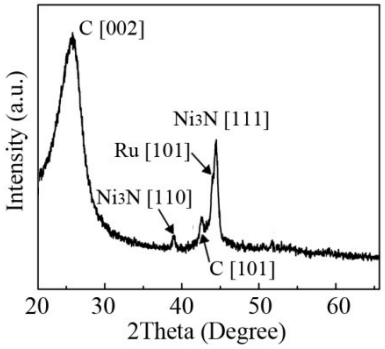


**Fig. S3** XRD pattern of the $Ni_3N$/Ru/NCAC composites.

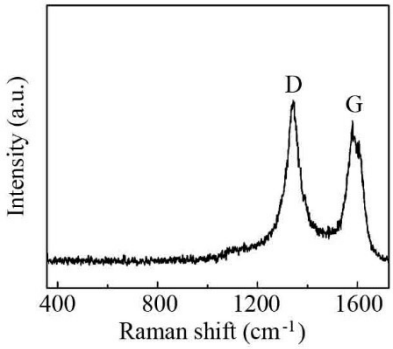


**Fig. S4** Raman spectrum of the $Ni_3N$/Ru/NCAC composites.

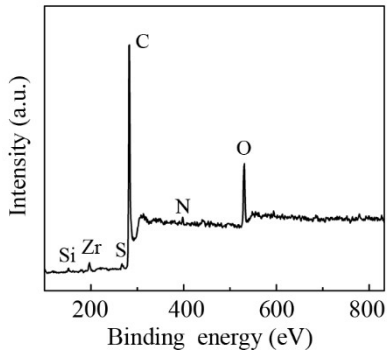


**Fig. S5** XPS spectrum of the CACs, showing that the CACs contain heteroatoms of Si, Zr, S and N.

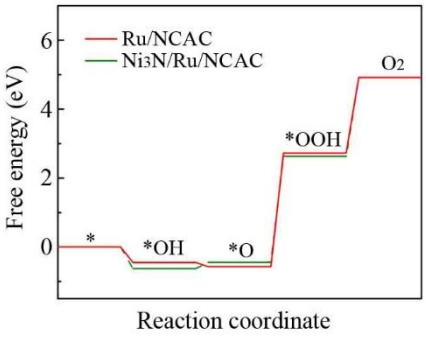


**Fig. S6** Calculated free energy diagrams of Ru/NCACs and $Ni_3N$/Ru/NCAC composites for the OER.

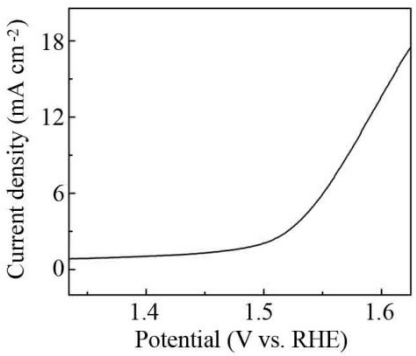


**Fig. S7** LSV curve of the $Ni_3N$/NCACs for OER, showing $\eta_{10}$ of 348 mV. This result reveals that $Ni_3N$/Ru/NCAC composites have a higher OER activity than $Ni_3N$/NCACs.

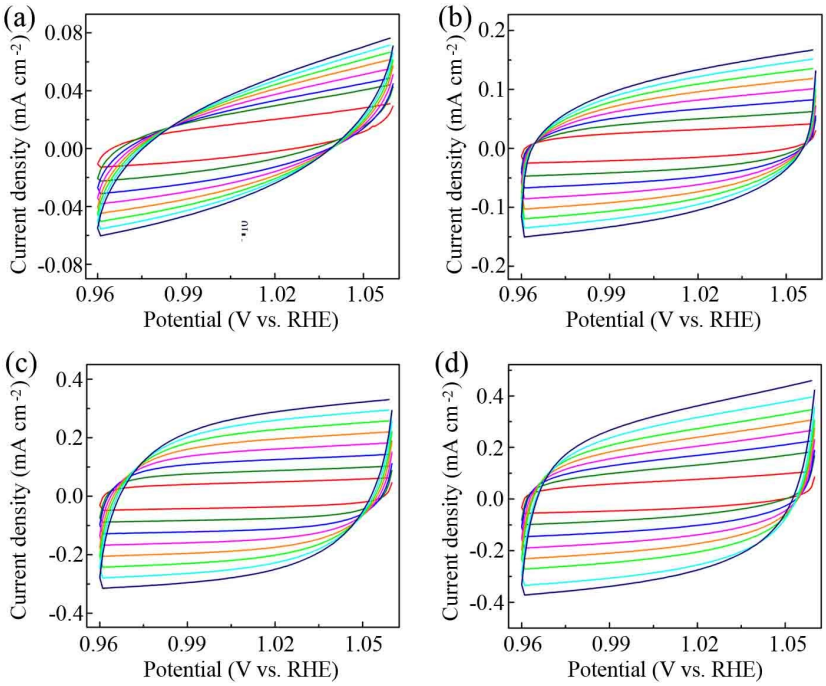


**Fig. S8** Cyclic voltammograms measured at different scan rates ranging from 2 to 16 mV $s^{-1}$: (a) CACs, (b) NCACs, (c) Ru/NCACs, and (d) $Ni_3N$/Ru/NCAC composites. The scanning potential range is from 0.96 V to 1.06 V vs. RHE.

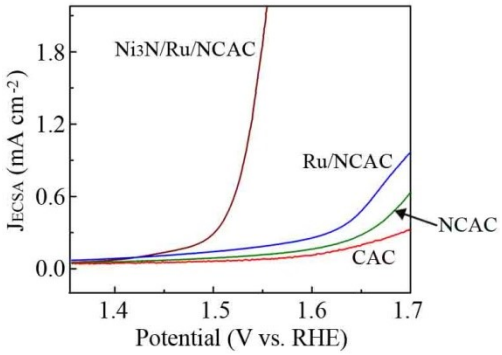


**Fig. S9** ECSA-normalized LSV curves of CACs, NCACs, Ru/NCACs and

$Ni_3N$/Ru/NCAC composites.

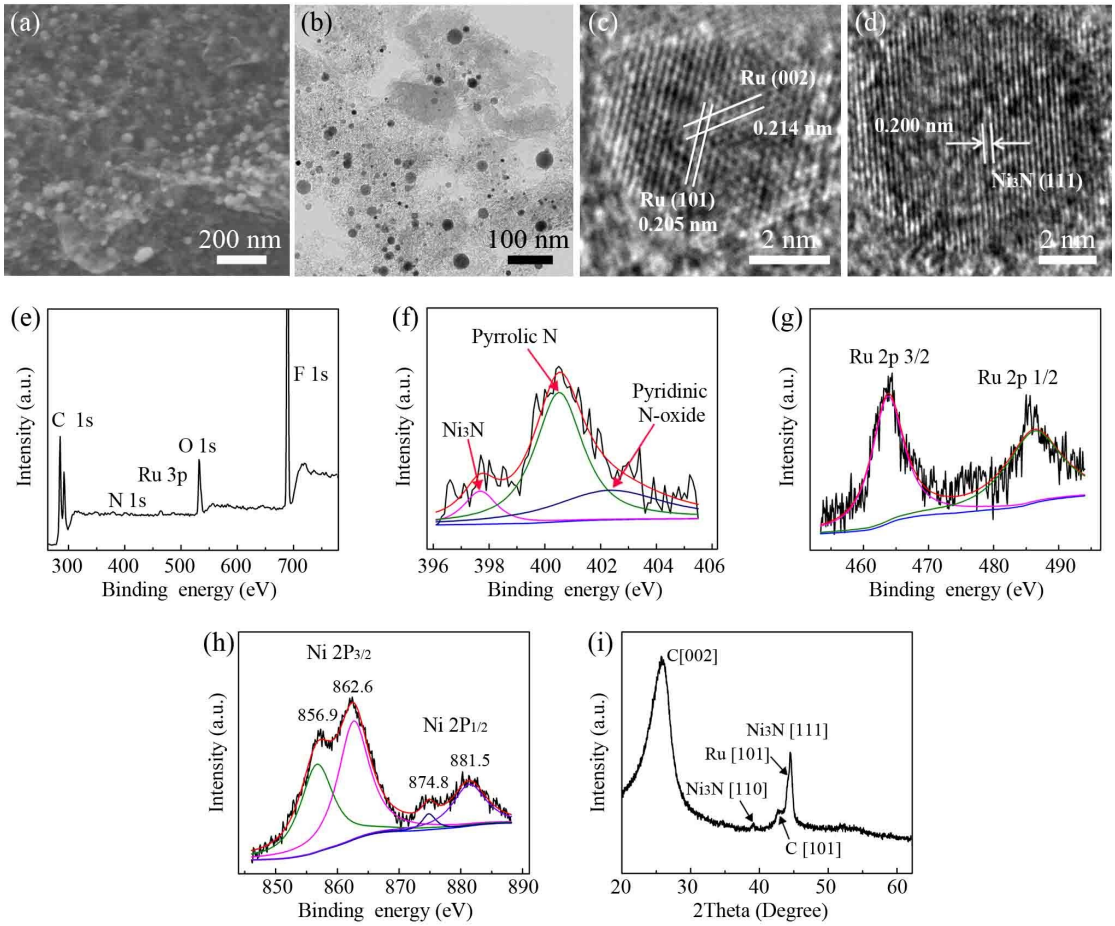


**Fig. S10** Characterization results of the $Ni_3N$/Ru/NCAC composites after the OER durability test. (a, b) SEM and TEM images, respectively. We can see that Ru and $Ni_3N$ nanoparticles remained on the NCACs. (c, d) HRTEM images of Ru and $Ni_3N$ nanoparticles, respectively. (e) XPS spectrum. The peaks at 291 and 688 eV correspond to $CF_x$ and F 1s, respectively.[2] The F elements were derived from the residual nafion on the $Ni_3N$/Ru/NCAC composites. High resolution XPS spectra: (f) N 1s, (g) Ru 2p, and (h) Ni 2p. From (f), we can see that the original pyridinic N was transformed into pyrrolic N (400.5 eV) after the OER stability test.[3] From (g), it can be observed that the peaks of Ru 2p 3/2 and Ru 2p 1/2 were at 463.7 and 486.4 eV, respectively. This result indicates the formation of $RuO_2$.[4] In (h), the peaks at 856.9 and 874.8 eV were ascribed to $Ni^{3+}$ 2p3/2 and $Ni^{3+}$ 2p1/2 of NiOOH, respectively. Hence, oxidization during the OER process resulted in transformation of $Ni_3N$ to NiOOH.[5,6] (i) XRD pattern. In comparison with the XRD pattern in Fig. S3, it is clear that oxidization of Ru and Ni elements happened only partially on surfaces of the Ru and $Ni_3N$ nanoparticles, and the main compositions of the $Ni_3N$/Ru/NCAC composites did not change.

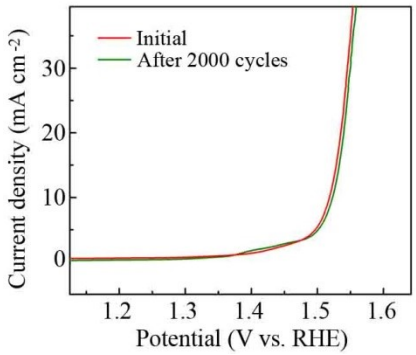


**Fig. S11** LSV curves of the $Ni_3N$/Ru/NCAC composites before and after 2000 CV cycles.

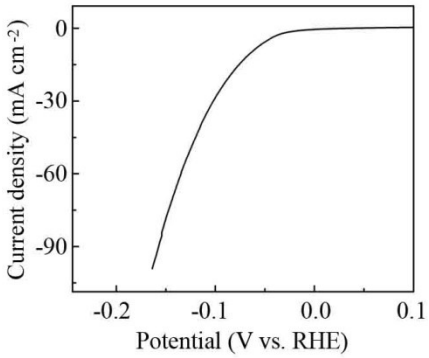


**Fig. S12** LSV curve of the $Ni_3N$/NCACs for HER, showing $\eta_{10}$ of 63 mV. This result reveals that $Ni_3N$/Ru/NCAC composites have a higher HER activity than $Ni_3N$/NCACs.

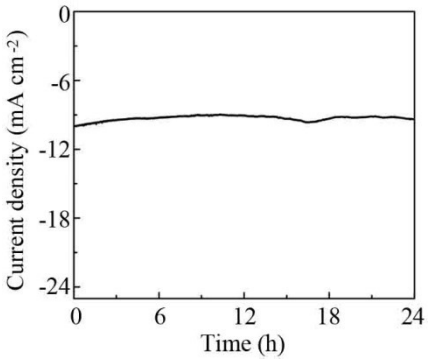


**Fig. S13** Chronoamperometric curves of the $Ni_3N$/Ru/NCAC composites at an overpotential of 42 mV in 1 M aq. KOH solution for HER.

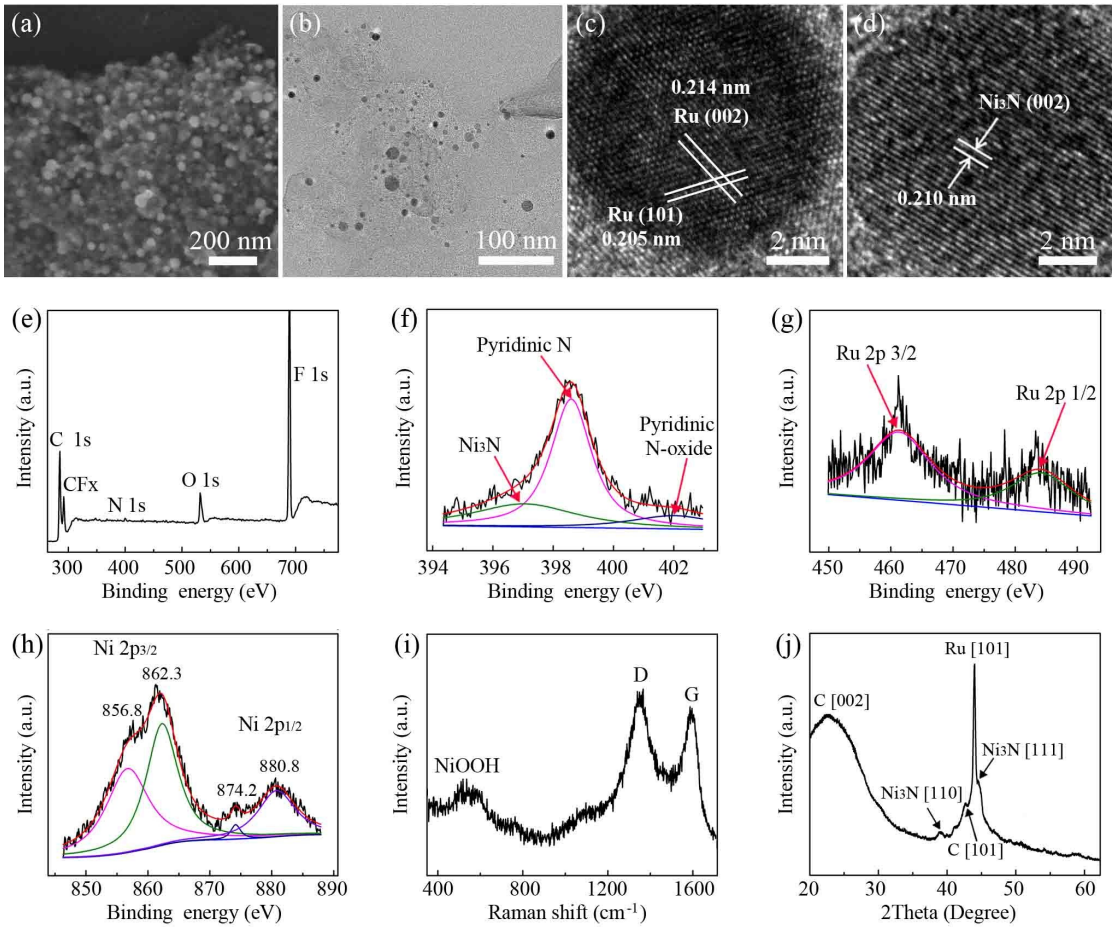


**Fig. S14** Characterization results of the $Ni_3N$/Ru/NCAC composites after the HER durability test. (a, b) SEM and TEM images, respectively. (c, d) HRTEM images of Ru and $Ni_3N$ nanoparticles, respectively. (e) XPS spectrum. High resolution XPS spectra: (f) N 1s, (g) Ru 2p, and (h) Ni 2p. From (g), it can be observed that the peaks of Ru 2p 3/2 and Ru 2p 1/2 were at 461.3 and 484 eV, respectively. This confirms that Ru elements were in the form of metallic Ru.[4] In (h), the high resolution XPS spectra of Ni 2p demonstrate almost the same peaks as those in Fig. S10h, indicating the formation of NiOOH after the HER stability test. (i) Raman spectrum. The peak at ~ 545 $cm^{-1}$ was attributable to the NiOOH,[5] confirming again the transformation of $Ni_3N$ into NiOOH during the HER process. (j) XRD pattern. In comparison with the XRD pattern in Fig. S3, it is clear that the formation of NiOOH only happened on surfaces of the $Ni_3N$ nanoparticles, and the main compositions of the $Ni_3N$/Ru/NCAC composites did not change.

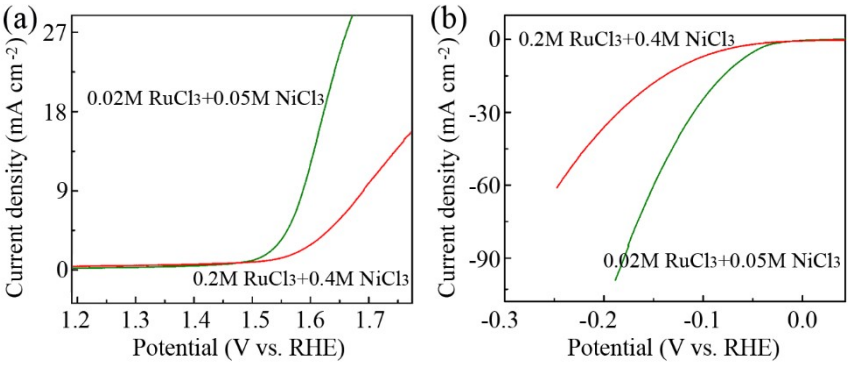


**Fig. S15** LSV curves of $Ni_3N$/Ru/NCAC composites: (a) OER and (b) HER. The concentrations of $RuCl_3$ and $NiCl_3$ in aqueous solutions used for the synthesis of $Ni_3N$/Ru/NCAC composites are marked in the diagrams.

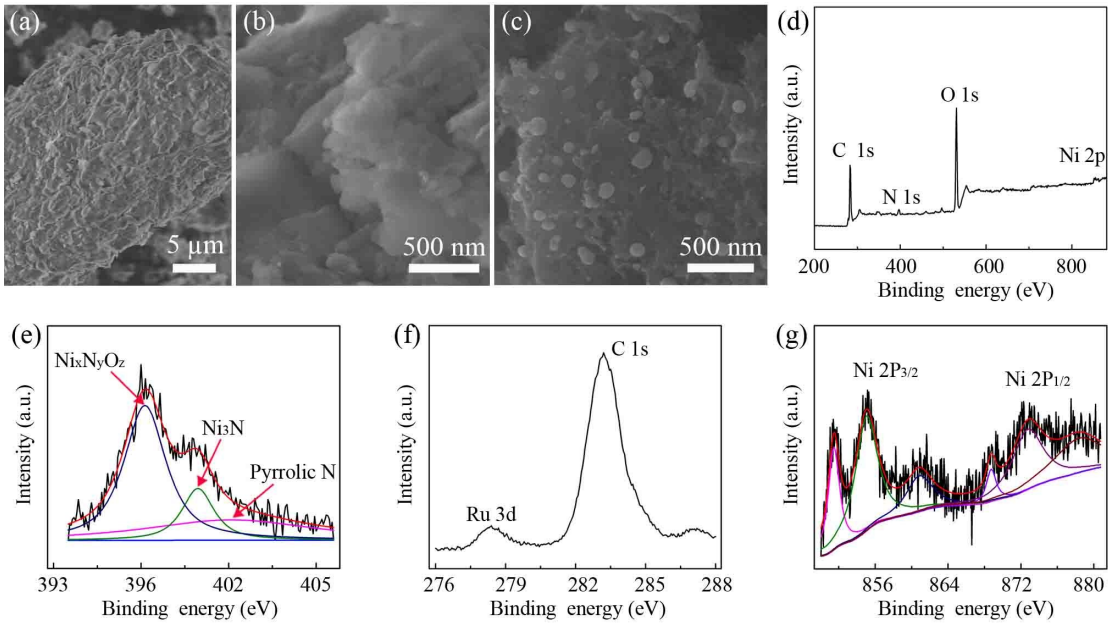


**Fig. S16** (a, b) SEM and high-magnification SEM images of wood-based activated carbons, respectively. (c-g) Characterization results of the $Ni_3N$/Ru/NWAC composites. (c) High-magnification SEM image. (d) XPS spectrum. High resolution XPS spectra: (e) N 1s, (f) Ru 3d, and (g) Ni 2p.

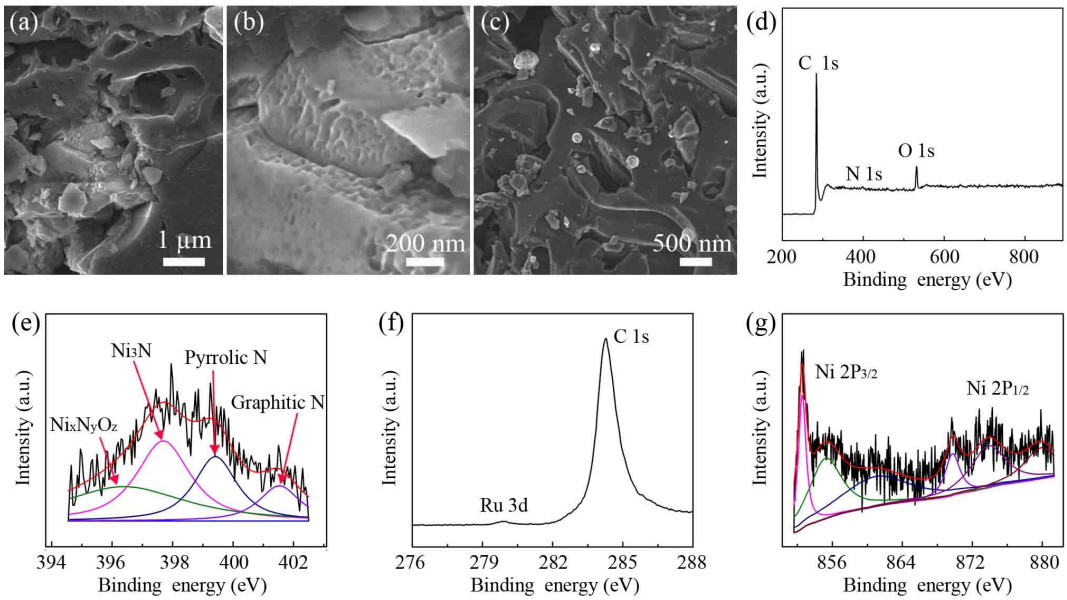


**Fig. S17** (a, b) SEM and high-magnification SEM images of coconut shell-based activated carbons, respectively. (c-g) Characterization results of the $Ni_3N$/Ru/NSAC composites. (c) High-magnification SEM image. (d) XPS spectrum. High resolution XPS spectra: (e) N 1s, (f) Ru 3d, and (g) Ni 2p.

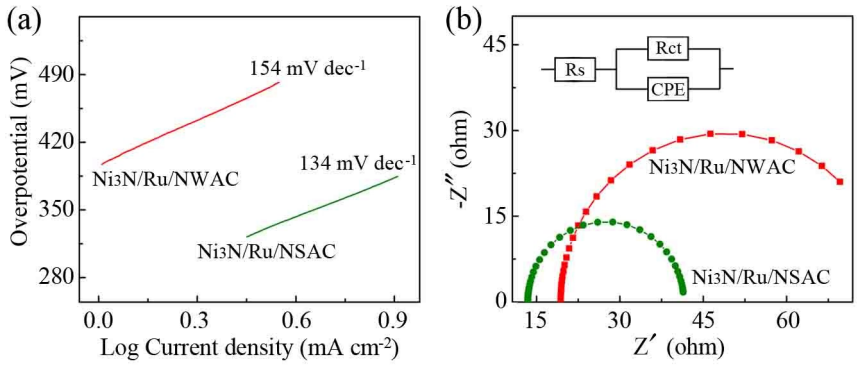


**Fig. S18** Tafel (a) and Nyquist plots (b) of the $Ni_3N$/Ru/NWAC and $Ni_3N$/Ru/NSAC composites for OER.

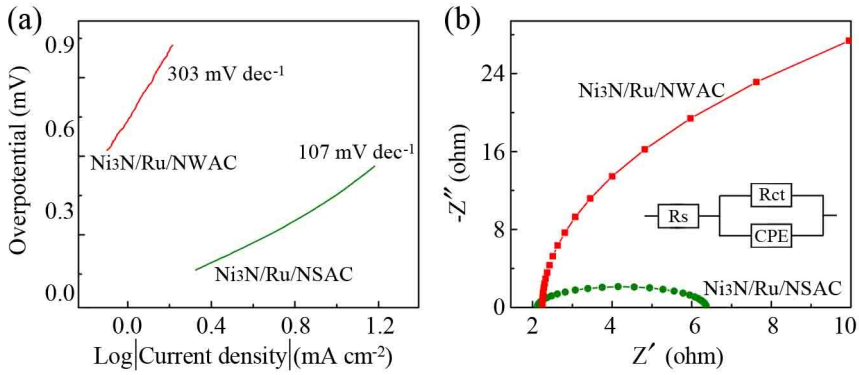


**Fig. S19** Tafel (a) and Nyquist plots (b) of the $Ni_3N$/Ru/NWAC and $Ni_3N$/Ru/NSAC composites for HER.

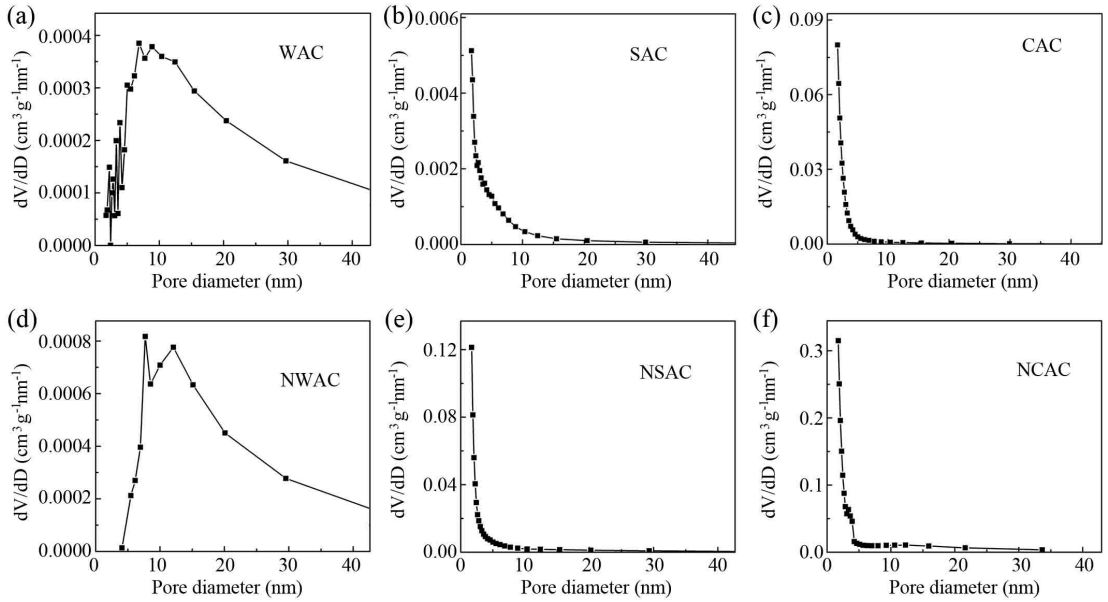


**Fig. S20** Pore size distribution curves: (a) WACs, (b) SACs, (c) CACs, (d) NWACs, (e) NSACs, and (f) NCACs.

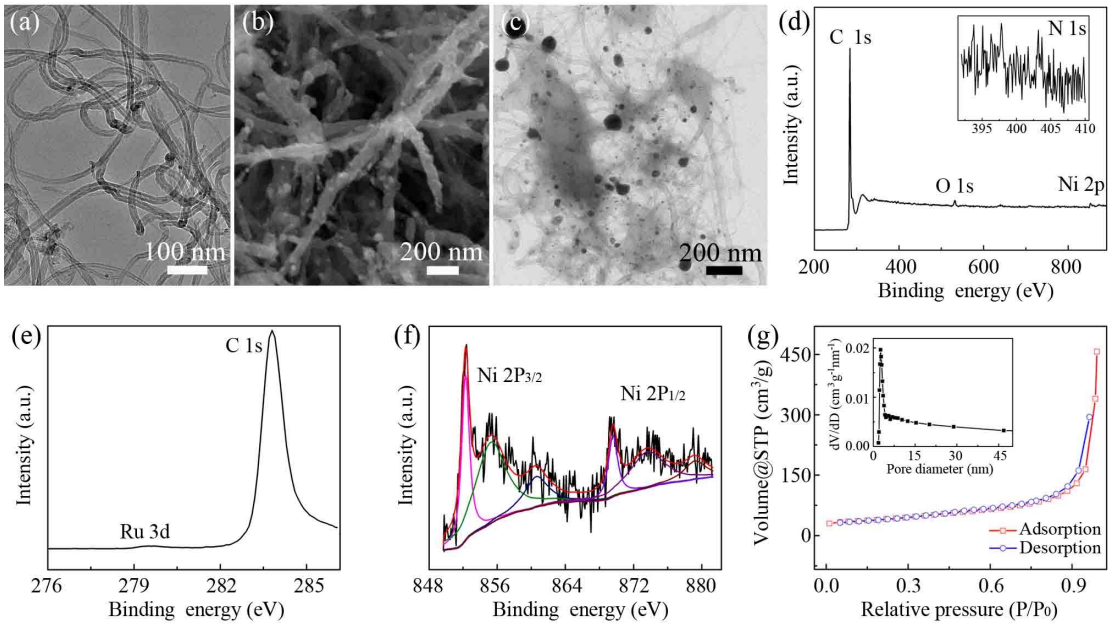


**Fig. S21** (a) TEM image of commercial CNTs. (b)-(g) Characterization results of the $Ni_3N$/Ru/NCNT composites. (b, c) High-magnification SEM and TEM images, respectively. (d) XPS spectrum. Inset: High resolution XPS spectra of N 1s. It can be observed that the CNTs had a low content of doped nitrogen. (e, f) High resolution XPS spectra of Ru 3d and Ni 2p, respectively. (g) Nitrogen adsorption-desorption isotherm of the $Ni_3N$/Ru/NCNT composites. Inset: Pore size distribution curve.

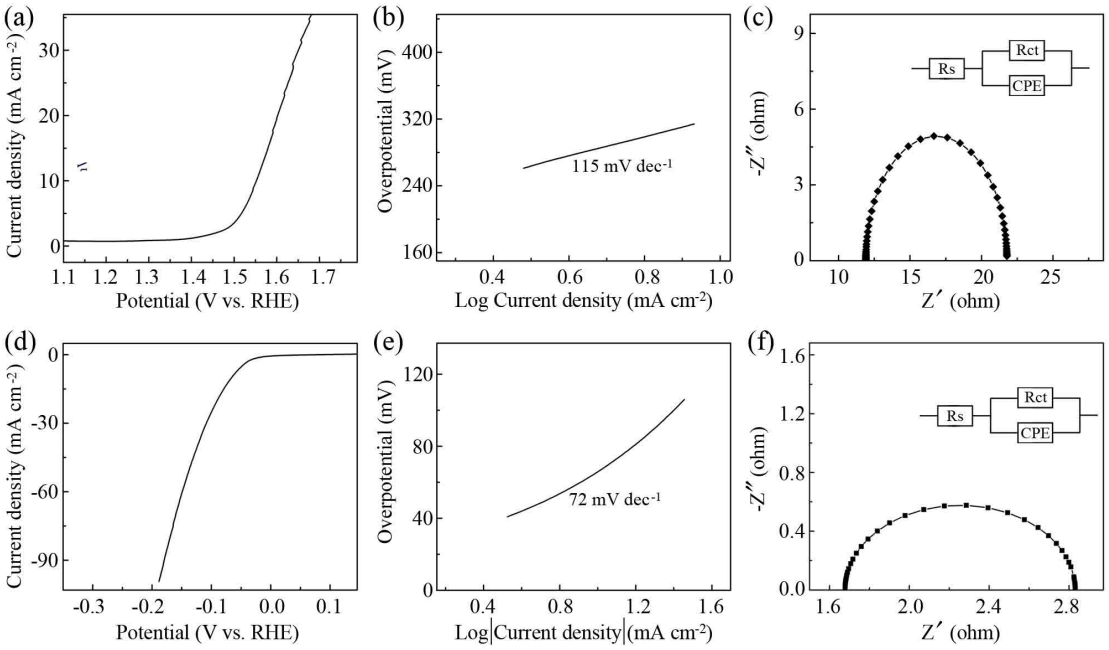


**Fig. S22** Electrochemical measurement results of the $Ni_3N$/Ru/NCNT composites: (a-c) OER and (d-f) HER. (a, d) LSV curves. Scan rate: 5 mV $s^{-1}$. (b, e) Tafel plots. (c, f) Nyquist plots.

**Table S1** Comparison of the activities of recently reported catalysts for OER

| Electrocatalysts | Overpotential at 10 mA $cm^{-2}$ (mV) | Tafel slope (mV $dec^{-1}$) | Electrolyte | Reference | Year |
|---|---|---|---|---|---|
| $Ni_3N$/Ru/NCAC composites | 288 | 60 | 0.1 M KOH | **This work** | |
| CoP/NCNHP | 310 | 70 | 1.0 M KOH | 7 | 2020 |
| NCNs | 410 | 142 | 0.1 M KOH | 8 | 2019 |
| $Co_4S_3/Mo_2C$-NSC | 268 | 61.2 | 1.0 M KOH | 9 | 2020 |
| $FeNi_3$@NC | 277 | 77 | 1.0 M KOH | 10 | 2020 |
| $La_{0.85}Ce_{0.15}NiO_3$ | 340 | 61 | 1.0 M KOH | 11 | 2021 |
| Co-$MoS_2/TiO_2$ | 317.5 | 125.9 | 1.0 M KOH | 12 | 2021 |
| Ni-bipy-MWNT | 310 | 35 | 0.1 M NaOH | 13 | 2020 |
| $Co_{5.47}$N@N-rGO | 350 | 80 | 0.1 M KOH | 14 | 2020 |
| $W_2N$/WC | 320 | 94.5 | 0.1 M KOH | 15 | 2019 |
| $Ni_3Fe$/Co-NC | 310 | 53 | 0.1 M KOH | 16 | 2018 |

**Table S2** Comparison of the activities of recently reported catalysts for HER

| Electrocatalysts | Overpotential at 10 mA $cm^{-2}$ (mV) | Tafel slope (mV $dec^{-1}$) | Electrolyte | Reference | Year |
|---|---|---|---|---|---|
| $Ni_3N$/Ru/NCAC composites | 42 | 59 | 1.0 M KOH | **This work** | |
| Co/N-CNT/VN | 63.4 | 62 | 1.0 M KOH | 17 | 2020 |
| $Co_4S_3/Mo_2C$-NSC | 82.5 | 61.8 | 1.0 M KOH | 9 | 2020 |
| $Co_9S_8$@N-S-HPC | 173 | 78 | 1.0 M KOH | 18 | 2019 |
| $CuMo_2ON$@NG | 81 | 47.3 | 1.0 M KOH | 19 | 2017 |
| Cu@NiFe LDH | 116 | 58.9 | 1.0 M KOH | 20 | 2017 |
| $Co_{0.97}Ti_{0.03}SP$ | 130 | 118 | 1.0 M KOH | 21 | 2020 |
| $Cu_{0.6}In_{0.4}NNi_3$ | 70 | 75 | 1.0 M KOH | 22 | 2020 |
| $NiWO_4/Ni_3S_2$ | 136 | 112 | 1.0 M KOH | 23 | 2020 |
| Ni-MoP | 162 | 102.6 | 1.0 M KOH | 24 | 2020 |
| RuCu NSs/C | 40 | 22.3 | 0.1 M KOH | 25 | 2019 |

**Table S3** Comparison of composites derived from different activated carbons

| Composites | N content (wt %) | Ru content (wt %) | Ni content (wt %) | BET surface area ($m^2/g$) |
|---|---|---|---|---|
| $Ni_3N$/Ru/NWAC | 3.3 | 1.4 | 3.8 | 6 |
| $Ni_3N$/Ru/NSAC | 2.4 | 0.5 | 1.9 | 174 |
| $Ni_3N$/Ru/NCAC | 2.9 | 0.3 | 2.7 | 853 |

**Table S4** Comparison of different activated carbons

| Activated carbons | BET surface areas before ammonia annealing ($m^2/g$) | BET surface areas after ammonia annealing ($m^2/g$) | BET surface area increase ($m^2/g$) | Mass loss (mg) |
|---|---|---|---|---|
| WACs | 7.2 | 8.8 | 1.6 | 35 |
| SACs | 75 | 733 | 658 | 140 |
| CACs | 534 | 1246 | 712 | 180 |

**Table S5** Comparison of the activities of recently reported catalysts for OWS

| Electrocatalysts | Cell voltage at 10 mA $cm^{-2}$ (V) | Electrolyte | Reference | Year |
|---|---|---|---|---|
| $Ni_3N$/Ru/NCAC composites | 1.55 | 1.0 M KOH | **This work** | |
| Ultrathin MOF array | 1.55 | 0.1 M KOH | 26 | 2017 |
| CoP/NCNHP | 1.64 | 1.0 M KOH | 7 | 2018 |
| NiSe nanosheets | 1.69 | 1.0 M NaOH | 27 | 2018 |
| $Ni_3N$/NiMoN | 1.54 | 1.0 M KOH | 28 | 2018 |
| CoFeZr oxides | 1.63 | 1.0 M KOH | 29 | 2019 |
| Ru-NiCoP/NF | 1.515 | 1.0 M KOH | 30 | 2020 |
| Co-$Co_2C$/CC | 1.63 | 1.0 M KOH | 31 | 2021 |
| CoP-InNC@CNT | 1.58 | 1.0 M KOH | 32 | 2020 |
| GH-BGQD | 1.61 | 0.1 M KOH | 33 | 2019 |
| POM@ZnCoS/NF | 1.56 | 1.0 M KOH | 34 | 2021 |

**References**


1 J. K. Nørskov, J. Rossmeisl, A. Logadottir, L. Lindqvist, J. R. Kitchin, T. Bligaard, H. Jónsson, *J. Phys. Chem. B* 2004, **108**, 17886.

2 C. Chen, G. Levitin, D. W. Hess, T. F. Fuller, *J. Power Sources*, 2007, **169**, 288.

3 Y. Ha, B. Fei, X. Yan, H. Xu, Z. Chen, L. Shi, M. Fu, W. Xu, R. Wu, *Adv. Energy Mater.*, 2020, **10**, 2002592.

4 J. Li, M. Huang, X. Chen, L. Kong, Y. Zhou, M. Wang, J. Li, Z. Wu, X. Xu, *Chem. Commun.*, 2020, **56**, 6802.

5 M. Chen, J. Qi, D. Guo, H. Lei, W. Zhang, R. Cao, *Chem. Commun.*, 2017, **53**, 9566.

6 X. Shang, K. Yan, Y. Rao, B. Dong, J. Chi, Y. Liu, X. Li, Y. Chai, C. Liu, *Nanoscale*, 2017, **9**, 12353.

7 Y. Pan, K. Sun, S. Liu, X. Cao, K. Wu, W. Cheong, Z. Chen, Y. Wang, Y. Li, Y. Liu, D. Wang, Q. Peng, C. Chen, Y. Li, *J. Am. Chem. Soc.*, 2018, **140**, 2610.

8 H. Jiang, J. Gu, X. Zheng, M. Liu, X. Qiu, L. Wang, W. Li, Z. Chen, X. Ji, J. Li, *Energy Environ. Sci.*, 2019, **12**, 322.

9 Y. Liu, X. Luo, C. Zhou, S. Du, D. Zhen, B. Chen, J. Li, Q. Wu, Y. Iru, D. Chen, *Appl. Catal. B: Environ.*, 2020, **260**, 118197.

10 D. Chen, J. Zhu, X. Mu, R. Cheng, W. Li, S. Liu, Z. Pu, C. Lin, S. Mu, *Appl. Catal. B: Environ.*, 2020, **268**, 118729.

11 Y. Sun, R. Li, X. Chen, J. Wu, Y. Xie, X. Wang, K. Ma, L. Wang, Z. Zhang, Q. Liao, Z. Kang, Y. Zhang, *Adv. Energy Mater.*, 2021,**11**, 2003755.

12 D. C. Nguyen, T. L. L. Doan, S. Prabhakaran, D. T. Tran, D. H. Kim, J. H. Lee, N. H. Kim, *Nano Energy*, 2021, **82**, 105750.

13 M. Tavakkoli, M. Nosek, J. Sainio, F. Davodi, T. Kallio, P. M. Joensuu, K. Laasonen, *ACS Catal.*, 2017, **7**, 8033.

14 X. Shu, S. Chen, S. Chen, W. Pan, J. Zhang, *Carbon*, 2020, **157**, 234.

15 J. Diao, Y. Qiu, S. Liu, W. Wang, K. Chen, H. Li, W. Yuan, Y. Qu, X. Guo, *Adv. Mater.*, 2020, **32**, 1905679.

16 B. Liu, Y. Wang, H. Peng, R. Yang, Z. Jiang, X. Zhou, C. Lee, H. Zhao, W. Zhang, *Adv. Mater.*, 2018, **30**, 1803144.

17 C. Huang, D. Wu, P. Qin, K. Ding, C. Pi, Q. Ruan, H. Song, B. Gao, H. Chen, P. K. Chu, *Nano Energy*, 2020, **73**, 104788.

18 S. Zhang, D. Zhai, T. Sun, A. Han, Y. Zhai, W. Cheong, Y. Liu, C. Su, D. Wang, Y.

Li, *Appl. Catal. B: Environ.*, 2019, **254**, 186.

19 J. Balamurugan, T. T. Nguyen, N. H. Kim, D. H. Kim, J. H. Lee, *Nano Energy*, 2021, **85**, 105987.

20 L. Yu, H. Zhou, J. Sun, F. Qin, F. Yu, J. Bao, Y. Yu, S. Chen, Z. Ren, *Energy Environ. Sci.*, 2017, **10**, 1820.

21 V. Q. Bui, A. Kumar, H. T. D. Bui, J. Lee, Y. Hwang, H. M. Le, Y. Kawazoe, H. Lee, *Chem. Mater.*, 2020, **32**, 9591.

22 J. Zhang, L. Zhang, L. Du, H. L. Xin, J. B. Goodenough, Z. Cui, *Angew. Chem. Int. Ed.*, 2020, **59**, 17488.

23 S. Huang, Y. Meng, Y. Cao, F. Yao, Z. He, X. Wang, H. Pan, M. Wu, *Appl. Catal. B: Environ.*, 2020, **274**, 119120.

24 W. Xiao, L. Zhang, D. Bukhvalov, Z. Chen, Z. Zou, L. Shang, X. Yang, D. Yan, F. Han, T. Zhang, *Nano Energy*, 2020, **70**, 104445.

25 Q. Yao, B. Huang, N. Zhang, M. Sun, Q. Shao, X. Huang, *Angew. Chem. Int. Ed.*, 2019, **58**, 13983.

26 J. Duan, S. Chen, C. Zhao, *Nat. Commun.*, 2017, **8**, 15341.

27 H. Wu, X. Lu, G. Zheng, G. W. Ho, *Adv. Energy Mater.*, 2018, **8**, 1702704.

28 A. Wu, Y. Xie, H. Ma, C. Tian, Y. Gu, H. Yan, X. Zhang, G. Yang, H. Fu, *Nano Energy*, 2018, **44**, 353.

29 L. Huang, D. Chen, G. Luo, Y. Lu, C. Chen, Y. Zou, C. Dong, Y. Li, S. Wang, *Adv. Mater.*, 2019, **31**, 1901439.

30 D. Chen, R. Lu, Z. Pu, J. Zhu, H. Li, F. Liu, S. Hu, X. Luo, J. Wu, Y. Zhao, S. Mu,

*Appl. Catal. B: Environ.*, 2020, **279**, 119396.

31 P. Wang, J. Zhu, Z. Pu, R. Qin, C. Zhang, D. Chen, Q. Liu, D. Wu, W. Li, S. Liu, J. Xiao, S. Mu, *Appl. Catal. B: Environ.*, 2021, **296**, 120334.

32 L. Chai, Z. Hu, X. Wang, Y. Xu, L. Zhang, T. Li, Y. Hu, J. Qian, S. Huang, *Adv. Sci.*, 2020, **7**, 1903195.

33 T. V. Tam, S. G. Kang, M. H. Kim, S. G. Lee, S. H. Hur, J. S. Chung, W. M. Choi, *Adv. Energy Mater.*, 2019, **9**, 1900945.

34 J. Gautam, Y. Liu, J. Gu, Z. Ma, J. Zha, B. Dahal, L. Zhang, A. N. Chishti, L. Ni, G. Diao, Y. Wei, *Adv. Funct. Mater.*, 2021, **31**, 2106147.